Nano Research

Open Access

Research Article

Depressing the H_2O_2 generation rate to enhance the durability of the hydroxide exchange membrane fuel cells

Shuxin Zhang[1], Yongjia Sheng[1], Jinjie Fang[2], Wei Zhu[1]✉, and Zhongbin Zhuang[1]✉

[1] *State Key Lab of Organic-Inorganic Composites and Beijing Advanced Innovation Center for Soft Matter Science and Engineering, Beijing University of Chemical Technology, Beijing 100029, China*
[2] *PetroChina Shenzhen New Energy Research Institute Co., Ltd., Shenzhen 518054, China*

Cite this article: *Nano Research*, **2025**, *18*, 94907340. https://doi.org/10.26599/NR.2025.94907340

ABSTRACT: The hydroxide exchange membrane fuel cells (HEMFCs) are considered promising due to their potential low cost. However, their unsatisfied stabilities hinder the widespread application of HEMFCs. Here, we confirm that the *in-situ* generated H_2O_2 takes serious influence on the degradation of the HEMFCs, and the more H_2O_2 generated the worse HEMFC stability. A mixed titanium oxide and ruthenium oxide doped by niobium (TiO_2-RuO_2-Nb_2O_5 (TRNO)) is synthesized and used as support for Pt to replace the commonly used carbon. The Pt/TRNO catalyst shows low H_2O_2 yield when used as oxygen reduction reaction (ORR) catalyst. By using Pt/TRNO as cathode, the fabricated HEMFC shows outstanding long-term durability. The cell voltage only decays 2.2%, discharging at a constant current density of 500 mA·cm^{-2} for 170 h, with a low decay rate of 76 μV·h^{-1}. These findings reveal that H_2O_2 yield is a key factor leading to the degradation of HEMFC, and the HEMFC stability could be improved by using the oxide supported catalysts with low H_2O_2 yield.

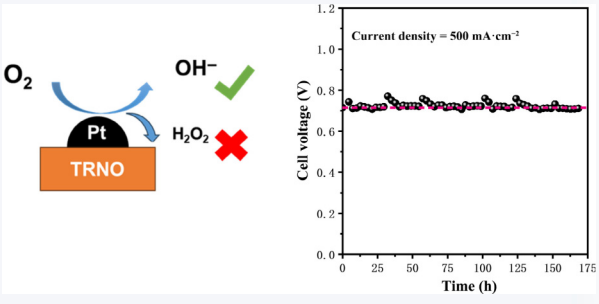

KEYWORDS: hydroxide exchange membrane fuel cell, durability, cathode, oxygen reduction reaction, hydrogen peroxide, support

1 Introduction

The usage of hydrogen energy offers a practical way to decrease reliance on fossil fuels and address environmental issues [1–4]. In the effort to develop a hydrogen economy, fuel cells play important roles [5–11]. The hydroxide exchange membrane fuel cells (HEMFCs), which are the structural analogue to the proton exchange membrane fuel cells (PEMFCs), have gained much attention due to their alkaline working environment that enables using platinum group metals (PGMs) free electrocatalysts and cheaper bipolar plates [12–16]. However, the most significant remaining challenge for the widespread use of the HEMFCs is their unsatisfied durability [17–20]. Most HEMFC membrane electrode assemblies (MEAs) have shown a substantial reduction in performance over the first 100–200 h of operation [21–23]. Even worse, the poor understanding of the key degradation mechanisms in operating cells further limits the development of HEMFC durability. The possible degradation source and effective strategies need further investigation to make HEMFC viable for practical applications [24, 25].

The polymer electrolyte plays key role for the satiability issue of the HEMFC [26–28]. The chemical stability issue of the HEMs, as well as the ionomers, includes the alkaline stability and oxidative stability [29, 30]. Generally, the HEMs and ionomers have similar chemical structures and have similar stability. With the development of over 20 years on the HEMs, their alkaline stabilities are notably improved. Many HEMs published in literatures show good alkaline stability [31–33]. Kim et al. reported polystyrene-b-poly(ethylene-co-butylene)-b-polystyrene (SEBS) HEM [31]. The SEBS HEM remained chemically stable after a 4-week alkaline stability test. Holdcroft et al. prepared a poly(arylene-imidazolium) (HMT-PMPI) HEM. This HEM exhibited minimal cation degradation after a 168-h alkaline stability test in 10 M KOH solution [32]. Yan et al. prepared poly(aryl piperidinium) (PAP) HEMs that maintained their ionic conductivity after 2000 h in 1 M KOH solution [33]. However, the oxidative stability of the HEMs and ionomers is still unclear. There is minimal research on

Received: December 27, 2024; **Revised:** February 21, 2025
Accepted: February 28, 2025

✉Address correspondence to Wei Zhu, zhuwei@mail.buct.edu.cn; Zhongbin Zhuang, zhuangzb@mail.buct.edu.cn

oxidative HEM and ionomer degradation, which is attributed to the generation of radicals during operation. In the past decades, the effects of radical species on the degradation of PEM have been well studied [34, 35]. The radicals are mainly formed from hydrogen peroxide (H_2O_2) resulted from a 2e⁻ oxygen reduction reaction (ORR) on the cathode side of the cell [36]. Note that while hydroperoxyl radicals is generated at low pH, the superoxide anion radical is favored at high pH [37, 38]. Superoxide anion radical has a long half-life in the highly alkaline environment and can cause significant oxidative damage to the ionomer nearby the catalysts as well as the membrane. Ramani et al. confirmed the HEM degradation in the presence of superoxide anion radical [39]. Therefore, it is essential to investigate the HEMFC performance degradation behavior caused by H_2O_2 and develop approaches that eliminate H_2O_2 to improve the longevity of HEMFC durability.

Here we test the HEMFC durability under different working condition with different H_2O_2 generating rate, in order to establish the correlation between the HEMFC stability and H_2O_2 yield. An oxide supported Pt catalyst (Pt/TiO_2-RuO_2 (TRO)-Nb_2O_5 (Pt/TRNO)) is synthesized and shows low H_2O_2 yield when catalyzing ORR, and an improved HEMFC stability was achieved by using this catalyst. The HEMFC using Pt/TRNO cathode exhibits remarkable durability of only 2.2% voltage decay after 170 h durability test at a constant current durability of 0.5 A·cm^{-2}, while the Pt/C HEMFC suffers from significant performance degradation.

2 Experimental

2.1 Chemicals

TiO_2 (AeroxidP25, Acros Organics), $RuCl_3 \cdot xH_2O$ (Ru content 45%–55%, Aladdin), $NbCl_5$ (99%, Aladdin), HNO_3 (65%, Aladdin), KOH (99.99%, Aladdin), $H_2PtCl_6 \cdot 6H_2O$ (99.95%, Macklin), HCOOH (≥ 88%, Aladdin), H_2O_2 (35%, Aladdin), Vulcan XC-72R (Cabot Corporation), Nafion solution (5%, DuPont), Pt/C (40%, Johnson Matthey), and gas diffusion layers (GDLs, SGL 28 BC) were used as received without further purification. The HEM (PiperION™ A15) and the ionomer were bought from Versogen. Ultrapure water (18.2 MΩ·cm, Mili-Q, Merck) was used in the synthesis of catalysts and electrochemical measurements.

2.2 Synthesis of the oxidized carbon (O–C)

150 mg of Vulcan XC-72R was dispersed in 100 mL of 12 M HNO_3 solution through ultrasonication for 20 min. The mixture was then heated to 80 °C with vigorous stirring at refluxed state for 2 h. Then, it was centrifuged and dispersed in water, followed by filtering and washing with plenty of water. Finally, the filter cake was dried by lyophilization.

2.3 Synthesis of the TiO_2-RuO_2-Nb_2O_5

In a typical synthesis, 80 mg of the TiO_2, 207 mg of $RuCl_3 \cdot xH_2O$, and 13.5 mg of $NbCl_5$ were dispersed in 100 mL of deionized water through ultrasonication for 30 min. Then, 0.5 M KOH solution was dropped into the mixture under vigorous stirring until the pH of the solution reached 7. The product obtained was then collected by vacuum filtration and washed with plenty of water. The black powders were then dried at 60 °C for 12 h and further calcined at 500 °C for 4 h in air to yield TRNO.

2.4 Synthesis of the Pt/TRNO catalyst

In a typical synthesis, 1060 μL of $H_2PtCl_6 \cdot 6H_2O$ aqueous solution (100 mg·mL^{-1}) and 60 mg of the obtained TRNO were dispersed in 50 mL of water by ultrasonication for 30 min. Then the solution was heat to 80 °C with vigorous stirring for 1 h, followed by adding 4 mL of HCOOH. Then, the mixture was kept under vigorous stirring for 2 h. The product obtained was then collected by vacuum filtration, washed several times with deionized water, and then dried in an oven at 60 °C. Then, it was ground and calcined at 200 °C for 8 h to obtain Pt/TiO_2-RuO_2-Nb_2O_5 catalyst.

2.5 Synthesis of the TiO_2-RuO_2

The TRO was prepared by the same method as TRO, except not using $NbCl_5$.

2.6 Synthesis of the Pt/TRO catalyst

The Pt/TRO catalyst was prepared by the same method as Pt/TRNO, except the support material was changed from TRNO to TRO.

2.7 Electrochemical measurements

The electrochemical measurements were performed on the CHI 760 electrochemical station (Shanghai Chenhua, China) with a standard three-electrode cell system. A homemade glass electrochemical cell equipped with three-electrode assembly was used. The saturated calomel electrode (SCE) and a graphite rod were used as the reference and counter electrodes, respectively. The catalyst ink was made by ultrasonically dispersing 1 mg of as-prepared catalyst in a mixed solution containing 100 μL of distilled water, 890 μL of ethanol, and 10 μL of 5 wt.% Nafion. Then, the catalyst ink was drop-cast on a glassy carbon electrode and used as the working electrode.

The rotating ring-disk electrode (RRDE) test was done by using a RRDE with a Pt ring with 6.25 mm inner diameter and 7.92 mm outer diameter to evaluate the ORR activity and the hydrogen peroxide yield (H_2O_2 (%)). During the RRDE test, the disc electrode was rotated in an O_2 saturated 0.1 M KOH electrolyte at 1600 rpm in a potential range from 0.05 to 1.05 V (vs. reversible hydrogen electrode (RHE)) with a scan rate of 5 mV·s^{-1}. The ring electrode was set to 1.2 V (vs. RHE). The mass activity (MA) of catalyst at 0.9 V was calculated by dividing the kinetic current by the corresponding Pt loading. The kinetic current was obtained by the following Eq. (1)

$$\frac{1}{I} = \frac{1}{I_k} + \frac{1}{I_d} \quad (1)$$

where I, I_k, and I_d represent the current at 0.9 V, the kinetic current at 0.9 V, and the diffusion limited current, respectively.

The hydrogen peroxide yield was calculated by the following Eq. (2)

$$H_2O_2(\%) = 200 \times \frac{I_{ring}/N}{I_{ring}/N + I_{disk}} \quad (2)$$

where I_{ring} is the ring current, I_{disk} is the disk current, I_{ring} and I_{disk} are absolute values, and N is the ring collection efficiency, which is $N = 0.37$ for the used RRDE.

The electrochemical active surface area (ECSA) of catalysts was quantified by the hydrogen underpotential deposition test. A cyclic voltammetry (CV) test was performed in Ar-saturated 0.1 M KOH

electrolyte between 0.03 and 1.05 V with a scan rate of 50 mV·s^{-1}, and the ECSA of Pt was calculated by the following Eq. (3)

$$\mathrm{ECSA} = \frac{Q_{\mathrm{H}}}{210\ \mu\mathrm{C}\cdot\mathrm{cm}^{-2} \times M_{\mathrm{Pt}}} \quad (3)$$

where Q_{H} is the charge associated with adsorption amount of H atoms at catalyst surface, 210 μC·cm^{-2} is the charge associated with the adsorption amount of one monolayer of H atoms on the Pt surface, and M_{Pt} is the loading of Pt on the working electrode.

Electrochemical impedance spectra (EIS) were recorded in the frequency range of 100 kHz to 0.1 Hz. ORR accelerated durability tests (ADTs) were conducted in O_2-saturated 0.1 M KOH electrolyte at 1600 rpm in a potential range from 0.60 to 1.00 V (vs. RHE) at a scan rate of 100 mV·s^{-1} for 10,000 cycles. The polarization curves before and after test were recorded by using rotating disk electrode (RDE) technique to evaluated the stability. All polarization curves were corrected with *iR* compensation.

2.8 HEMFC fabrications and tests

Catalyst ink was prepared by mixing catalyst with PAP-TP-85 (5 wt.%, Versogen) ionomers diluted by isopropanol/water (25:1) solvent and then sonication for 3 h in ice water bath. The commercial Pt/C (HiSpec 4000, 40 wt.% Pt, Johnson Matthey) was used as the anode catalyst with the loading of 0.4 $mg_{Pt}\cdot cm^{-2}$, and the synthesized Pt/TRNO catalyst or the commercial Pt/C was used as the cathode catalyst with the loading of 0.4 $mg_{Pt}\cdot cm^{-2}$. For the Pt/TRNO cathode, the 40 wt.% (of catalyst mass) Vulcan XC-72R was added to the cathode ink. For the Pt/C+O–C cathode, the loading of O-Vulcan was 100 wt.% relative to the Pt/C. The catalyst ink was sprayed onto both sides of PiperION™ A15 membrane (17 μm) to fabricate a catalyst coated membrane (CCM) with the electrode area of 5 cm^2. The prepared CCM was soaked in 3 M KOH for 12 h to exchange Cl^- to OH^- and then washed with deionized water to remove the excess KOH. The washed CCM was assembled with a fluorinated ethylene propylene (FEP) gasket, a GDL (SGL 28 BC), a graphite bipolar plate with 5 cm^{-2} flow field and a metal current collector for each side to complete the full HEMFC. Then, all of the HEMFC were controlled using a Scribner 850e equipped with a backpressure module. During the HEMFC tests, the fuel cell was activated and tested by scanning current method and the cell polarization curves were recorded. Then, the HEMFC was further subjected to the durability test, where the cell was held at constant current density. During this durability test, the cell temperature was set at 80 °C while the dew points of the reacting gases were initially set to 78 °C at the anode and 79 °C at the cathode.

2.9 Characterization

The ^{1}H nuclear magnetic resonance (^{1}H NMR) spectra were used to analyze the precise structure of membranes. A Brunauer–Emmett–Teller (BET) surface area analyzer (Micromeritics ASAP 2460 system) was used to calculate the BET specific surface area by a multipoint analysis of nitrogen desorption isotherms. Transmission electron microscopy (TEM) images were recorded on a Hitachi 7700 transmission electron microscopy. High-resolution TEM (HRTEM) and energy dispersive spectroscopy (EDS) mapping were performed on a JEOL JEM-2100F transmission electron microscopy. The X-ray photoelectron spectroscopy (XPS) spectra were obtained on a Thermo Fisher ESCALAB 250Xi spectrometer with a monochromatic Al Kα X-ray source. The binding energies derived from XPS measurements were calibrated to the C 1s at 284.8 eV. The powder X-ray diffraction (XRD) patterns were profiled on a Rigaku D/Max 2500 VB2+/PC X-ray powder diffractometer using Cu Kα radiation (λ = 0.154 nm), and all of the diffraction data were collected in a 2θ range from 10° to 90° at a scanning rate of 5 °·min^{-1}. Inductively coupled plasma-optical emission spectroscopy (ICP-OES, Optima 7300 DV, Perkin Elmer) was used to determine the metal contents.

3 Results and discussion

3.1 The *in-situ* generated H_2O_2 impacts the HEMFC stability

We first examined the effect of the H_2O_2 on the HEM stability. To qualitatively determine the effect of H_2O_2 on the HEM, we employed an *ex-situ* stability test of HEM. PAP HEM (PAP-TP-85) were immersed into 5 wt.% H_2O_2 solution for 24 h. The degradation degree of the peak assignments of PAP-TP-85 is indicated in Fig. 1 [33]. The peak at 3.15 ppm is the methyl hydrogens on piperidinium cation, and the peaks at the range of 7.46–7.79 ppm are the hydrogens on triphenyl rings. We calculated the grafting degree of PAP polymers before and after test by the ratio of peak areas of the methyl hydrogens on piperidinium cationic groups and the hydrogens on the triphenyl rings. The grafting degrees were found to be 85% and 53% before and after the test. It indicated that PAP membranes underwent remarkable piperidinium cationic group degradation in the presence of H_2O_2. The mechanical properties of membrane also have deteriorated after stability test. These results indicated that H_2O_2 severely impacts the stability of the HEM.

Next, we examined effect of the generated H_2O_2 on the MEA stability. When the HEMFCs work, cathode occurs in the ORRs. Ideally, the oxygen undergoes 4e$^-$ reduction to generate water. However, there are still some oxygen undergoes 2e$^-$ reduction to form H_2O_2 [40]. Figure 2(a) shows the linear sweep voltammetry (LSV) curves of the Pt/C catalyst measured by RRDE test, and the collected ring and disk currents can be used to calculate the H_2O_2

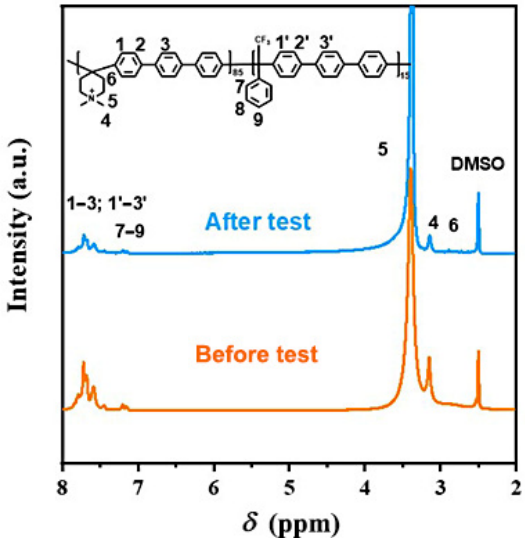

Figure 1 ^{1}H NMR spectra of PAP-TP-85 HEM before and after stability test. Dimethyl sulfoxide (DMSO)-d6 was used as the NMR solvent (2.50 ppm) and D_2O also remained in the polymer sample (3.33 ppm).

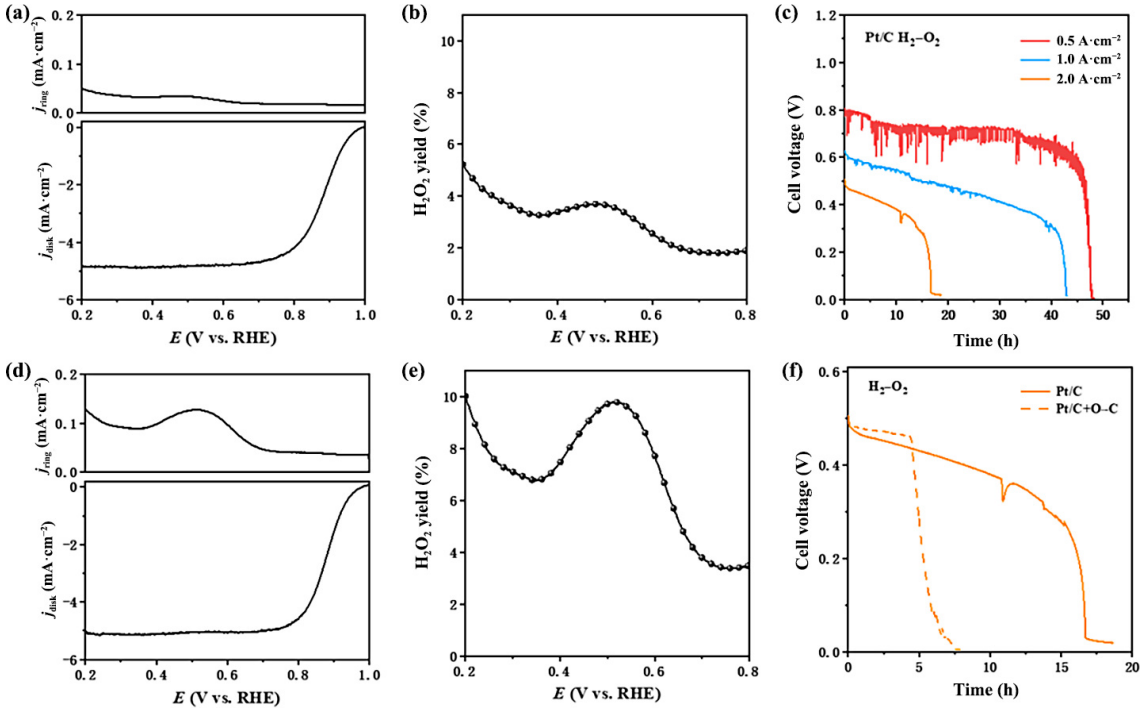

Figure 2 (a) Disk and ring current density of the Pt/C RRDE results tested in O_2-saturation 0.1 M KOH. (b) The H_2O_2 yield of the Pt/C. (c) H_2/O_2 HEMFCs durability test at various current densities of 0.5, 1.0, and 2.0 A·cm^{-2} with Pt/C (0.4 mg$_{Pt}$·cm^{-2}) in cathode and Pt/C (0.4 mg$_{Pt}$·cm^{-2}) in anode. The cell, cathode, and anode humidifier temperatures were 80, 78, and 79 °C, respectively. The anode and cathode were flowed with 0.4 L·min^{-1} of H_2 and 0.4 L·min^{-1} of O_2, respectively. The backpressures were 150 kPa (gauge) for both sides. (d) Disk and ring current density of the Pt/C+O–C RRDE results tested in O_2-saturation 0.1 M KOH. (e) The H_2O_2 yield of the Pt/C+O–C. (f) H_2/O_2 HEMFCs durability test at current densities of 2.0 A·cm^{-2} with Pt/C and Pt/C+O–C (0.4 mg$_{Pt}$·cm^{-2}) in cathode. The anode for the HEMFCs was 0.4 mg$_{Pt}$·cm^{-2} Pt/C. The cell, anode and cathode humidifier temperatures were 80, 78, and 79 °C, respectively. The anode and cathode were flowed with 0.4 L·min^{-1} of H_2 and O_2, respectively. The backpressures were 150 kPa (gauge) for both sides.

yield. Figure 2(b) shows the H_2O_2 yield of the Pt/C catalyst. Although the H_2O_2 yield is low (< 6%), H_2O_2 is clearly detected during the ORR process. We observed that the H_2O_2 yield of the Pt/C catalyst during oxygen reduction is potential dependent. The H_2O_2 yield increases with the decrease of the potential. We fabricated MEA using Pt/C as the cathode, and its polarization curve is shown in Fig. S1 in the Electronic Supplementary Material (ESM). We test the MEA stability at different cell voltages to study the impact of H_2O_2. The HEMFCs with same MEAs structures were operated at various current densities (0.5, 1.0, and 2.0 A·cm^{-2}) and studied their lifetime (Fig. 2(c)). Because the current densities changed, the cell voltages varied at different test conditions. At low current density, the cathode potential was high, which resulted in lower H_2O_2 yield. The HEMFC lasted 48 h before its failure. However, when the current densities increased, the durability of the HEMFC reduced. The durability reduced to 43 and 18 h when the current densities were 1.0 and 2.0 A·cm^{-2}, respectively. It suggests that the higher H_2O_2 yield leads to worse HEMFC stability.

To further investigate the impact of H_2O_2 on HEMFC stability, we fabricated MEA using a cathode catalyst with enlarged H_2O_2 yield. It was reported that O–C can improve the selectivity of 2e$^-$ ORR [41]. The O–C was synthesized through the nitric acid treatment, and it indeed shows higher H_2O_2 yield (Fig. S2 in the ESM). We blend the Pt/C with O–C to increase the H_2O_2 yield of the cathode. The LSV curves of the Pt/C catalyst mixed with O–C tested by RRDE are shown in Fig. 2(d). Figure 2(e) shows the H_2O_2 yield of the Pt/C mixed with O–C (Pt/C+O–C). Increased H_2O_2 yield compared with that for Pt/C was found in the whole tested potential region. For example, the H_2O_2 yield increased from 2.54% to 7.62% at 0.6 V vs. RHE when Pt/C was mixed with O–C. The HEMFC durability of the MEA using Pt/C+O–C as cathode was further studied. The Pt/C+O–C HEMFC delivered a current density of 959 mA·cm^{-2} at 0.65 V (Fig. S1 in the ESM), which indicated that the introduction of the O–C does not impact the cell performance significantly. However, as shown in Fig. 2(f) for the durability test, the Pt/C+O–C HEMFC failed at 8 h after constant discharge at the current density of 2.0 A·cm^{-2}, much shorter than the Pt/C HEMFC (18 h). The results demonstrate that the H_2O_2 yield at cathode significantly impacts the HEMFC stability, and the higher the H_2O_2 yield, the worse the stability.

3.2 Synthesis and characterization of the Pt/TRNO electrocatalyst

Based on the anterior discussions, we proposed that the HEMFC stability could be improved by depressing the H_2O_2 yield of the cathode catalysts. We replaced the commonly carbon supports to oxides, in order to reduce the H_2O_2 yield. We selected titanium oxide as the substrate due to its excellent electrochemical stability. To enhance the electrical conductivity of the support, ruthenium oxide was introduced as the secondary component, and niobium was selected as a dopant to further promote its conductivity.

Briefly, the TRNO support was synthesized by a simple wet chemical approach. BET adsorption/desorption isotherms disclose that the TRNO support possesses a relatively high surface area of 57 m^2·g^{-1} (Fig. S3 in the ESM). Figure 3(a) shows the XRD patterns of TRNO support. All the diffraction peaks can be assigned either

anatase TiO_2 (JCPDS No. 21-1272) or rutile RuO_2 (JCPDS No. 40-1290) without peaks from Nb-oxides. It suggests that the TRNO support is Nb-doped TiO_2 and RuO_2 mixture. The high-resolution XPS spectra of TRNO suggest the interaction in the oxide mixture (Figs. S4–S6 in the ESM). For the Ti 2p spectra, it shows a 0.4 eV positive shift compared with pristine TiO_2. For the Ru 3d spectra, it shows a 0.5 eV negative shift compared with pristine RuO_2. It suggests the electron transfer from TiO_2 to RuO_2. The Nb 3d spectra demonstrate the slightly high valance state of the Nb in TRNO compared with Nb_2O_5, probably due to the doped structure.

Subsequently, Pt nanoparticles were deposited on the oxide support by the reduction of H_2PtCl_6 with HCOOH [42]. Figure 3(a) shows the XRD patterns of the Pt/TRNO electrocatalyst. Compared with pattern for TRNO support, additional peaks at 39.76°, 46.24°, and 67.45° appear, which are attributed to the Pt (111), (200), and (220) planes, respectively. No distinct changes for the peaks from the TRNO support are found, indicating that the TRNO support does not change after deposition of Pt. The elemental contents were tested by ICP-OES, and the mass loading of Pt, Ti, Ru, and Nb in Pt/TRNO were ca. 39.4 wt.%, 13.3 wt.%, 23.7 wt.%, and 1.3 wt.%.

Figure 3(b) shows the Pt 4f high-resolution XPS spectra for the Pt/TRNO and commercial Pt/C. It is noted that the binding energy of the Pt 4f peaks for Pt/TRNO shifted negatively (0.4 eV) compared with that for Pt/C, which can be attributed to metal support interaction (MSI). The negatively shifted binding energy in Pt/TRNO leads to the lowered d-band center, which is beneficial for promoted ORR activity [43, 44]. Figure 3(c) shows the TEM images of the Pt/TRNO electrocatalyst. Pt nanoparticles were uniform dispersion the support, with the size mainly distributed in range of 4–6 nm. HRTEM image of the Pt/TRNO (Fig. 3(d)) revealed lattice fringes of 0.227, 0.238, and 0.315 nm, which are corresponded to the (111) plane of the Pt, (004) plane of the TiO_2, and (110) plane of the RuO_2, respectively. Furthermore, energy-dispersive X-ray spectroscopy confirmed the uniform dispersion of the Pt, Ru Ti, and Nb elements (Fig. S7 in the ESM).

3.3 ORR activity and H_2O_2 yield of the Pt/TRNO catalyst

We evaluated the ORR activity and H_2O_2 yield of the Pt/TRNO catalyst using the RRDE technique in O_2-saturated 0.1 M KOH electrolyte. The commercial Pt/C was tested under the same conditions for comparison. Figure 4(a) shows the LSV curves of the Pt/TRNO and the Pt/C using the same loading of the Pt (20 μg·cm^{-2}). Different from the lower ORR activity of Pt/TRO (Fig. S8(a) in the ESM), the Pt/TRNO catalyst shows the half-wave potential ($E_{1/2}$) of 0.873 V (vs. RHE, the same hereafter), which is similar to that for the Pt/C catalyst ($E_{1/2}$ = 0.878 V). ECSA was quantified by the hydrogen underpotential deposition tests, as shown in Fig. S9 in the ESM. Their specific activity (SA) and MA at

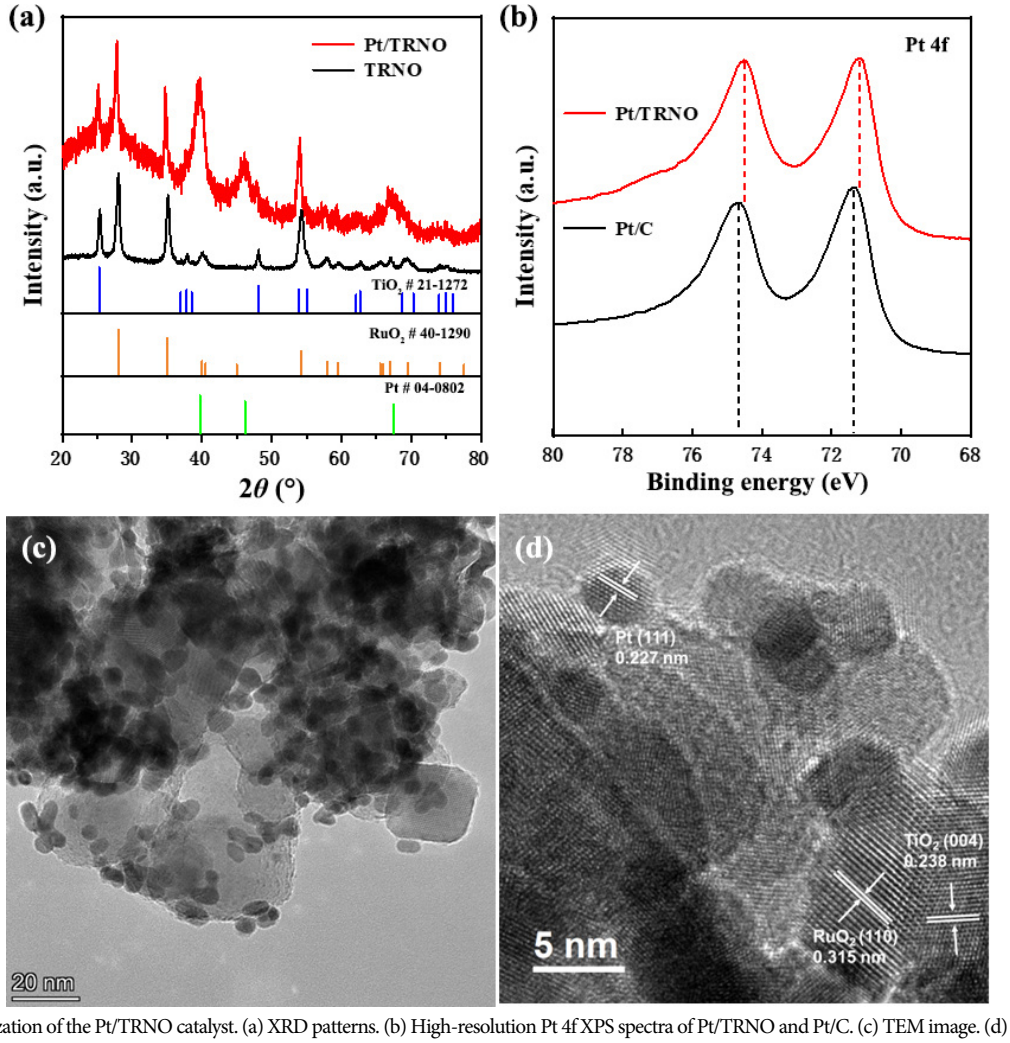

Figure 3 Characterization of the Pt/TRNO catalyst. (a) XRD patterns. (b) High-resolution Pt 4f XPS spectra of Pt/TRNO and Pt/C. (c) TEM image. (d) HRTEM image.

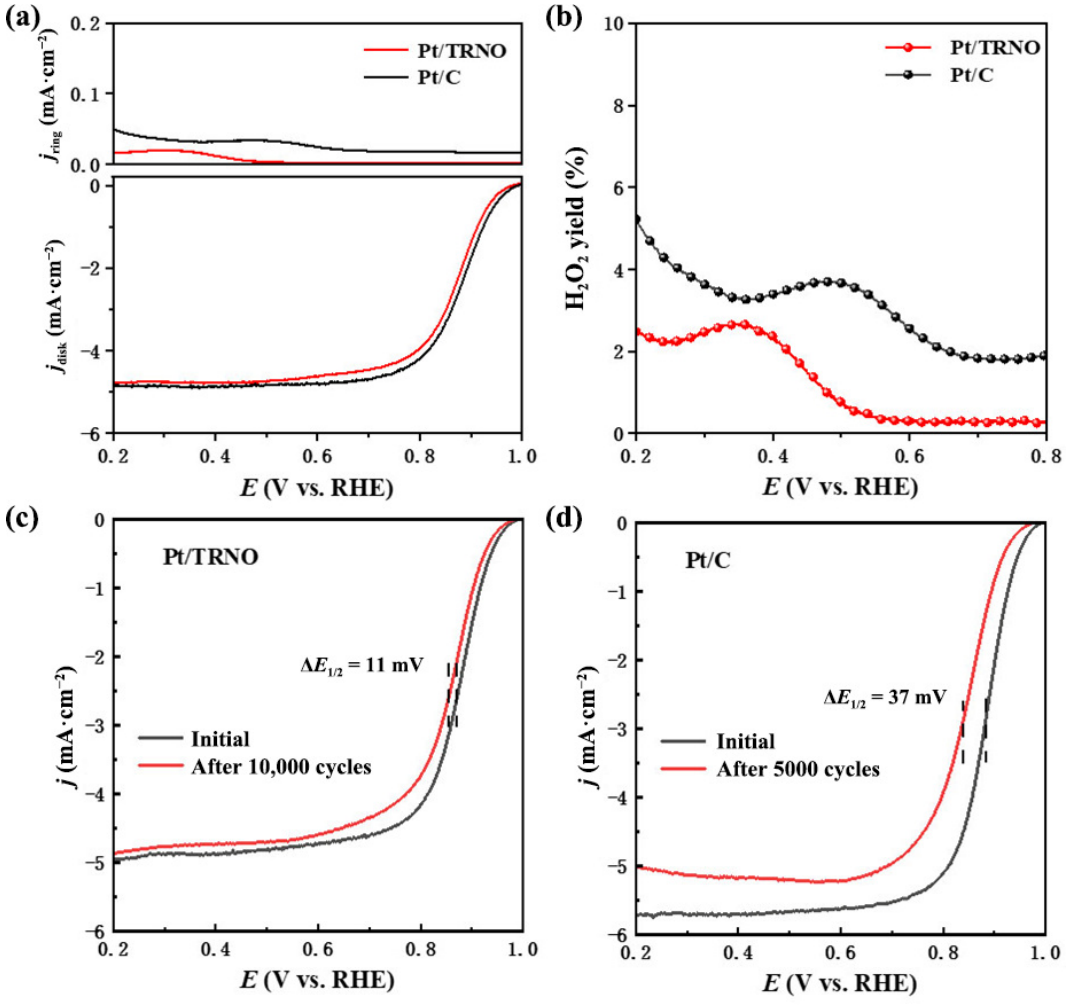

Figure 4 ORR performance and stability in 0.1 M KOH solution. (a) Disk and ring current density of the Pt/TRNO and Pt/C RRDE results tested in O_2-saturation 0.1 M KOH. (b) The H_2O_2 yield of the Pt/TRNO and Pt/C. ((c) and (d)) Disk current density of Pt/TRNO and Pt/C RDE results tested in O_2-saturation 0.1 M KOH before and after the potential cycling.

0.9 V are further shown in Table S1 in the ESM. The Pt/TRNO catalyst shows the SA of 0.28 mA·cm^{-2} and MA of 0.11 A·mg$_{Pt}^{-1}$, which is similar to that for the Pt/C catalyst (SA of 0.33 mA·cm^{-2} and MA of 0.18 A·mg$_{Pt}^{-1}$), suggesting the similar ORR activity. Figure 4(b) shows the H_2O_2 yield of the Pt/TRNO and Pt/C. The Pt/TRNO shows ultra-low H_2O_2 yield, which is only 0.31% at 0.6 V. Compared with that for Pt/C, the H_2O_2 yield for Pt/TRNO depresses clearly.

We also synthesized the undoped TRO supported Pt (Pt/TRO) to study the effect of Nb (synthetic procedure shown in experimental section, TEM images and XRD pattern shown in Fig. S10 in the ESM). The ORR polarization curve, as well as the H_2O_2 yield of the Pt/TRO, is shown in Fig. S8 in the ESM. The Pt/TRO displayed slightly lower ORR performance than Pt/TRNO, indicated by its lower $E_{1/2}$, as well as the MA and SA (summarized in Table S1 in the ESM). More important, the Pt/TRO exhibits higher H_2O_2 yield, which is 1.44% at 0.6 V, 4.5 times higher than that for Pt/TRNO. It suggests that the Nb doping is beneficial for promoting the ORR performance and also depresses the H_2O_2 generation.

We further evaluated the stability of the Pt/TRNO catalyst by CV cycles between 0.6 and 1.0 V with a scan rate of 100 mV·s^{-1} in O_2-saturated 0.1 M KOH electrolyte. As shown in Figs. 4(c) and 4(d), after 10,000 cycles, the $E_{1/2}$ for Pt/TRNO catalyst only decreased for 11 mV. In comparison, the $E_{1/2}$ of Pt/C catalyst loses 37 mV after only 5000 cycles. These results indicated that the Pt/TRNO catalyst has a higher stability than that of the Pt/C catalyst.

3.4 HEMFC performance and stability of the MEA using Pt/TRNO cathode

The synthesized Pt/TRNO catalyst was used as cathode catalyst to fabricate the HEMFC, and the commercial Pt/C was employed as anode catalyst. Figure 5(a) displays the polarization curve and power density curve of HEMFCs using Pt/TRNO catalyst as the cathode catalyst feeding with H_2/O_2. The Pt/TRNO HEMFC delivers a peak power density (PPD) of 1205 mW·cm^{-2}, which is slightly lower than the HEMFC employing Pt/C catalyst as cathode, probably due to the lower conductivity of the TRNO than carbon support. The Pt/TRNO HEMFC is able to deliver a current density of 1200 mA·cm^{-2} at 0.65 V, which is similar to that for Pt/C HEMFC (1364 mA·cm^{-2}) and higher than that for Pt/TRO HEMFC (495 mA·cm^{-2}, as shown in Fig. S11 in the ESM), indicating that Pt/TRNO has very promising performance in typical fuel cell operating voltage. The HEMFC using oxide supported catalysts

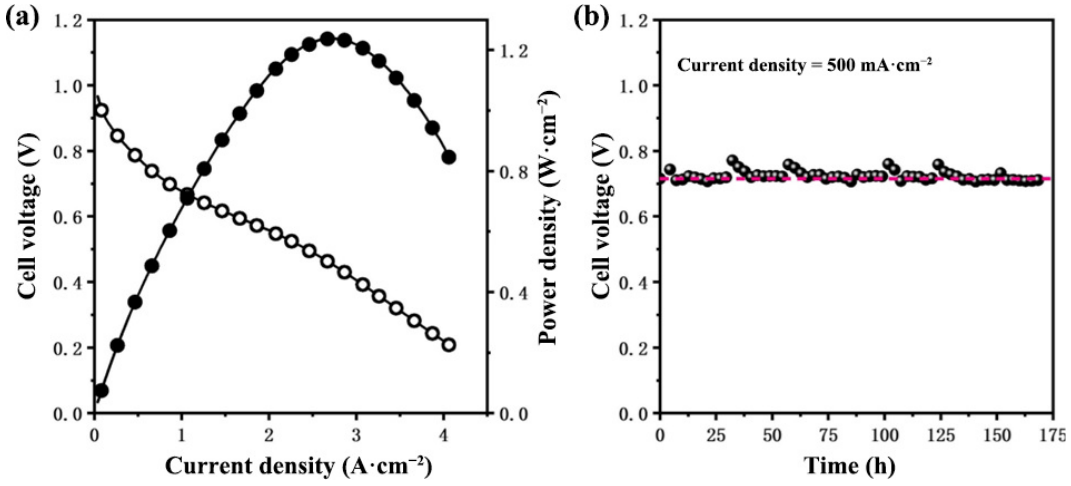

Figure 5 HEMFC performance and durability of the Pt/TRNO catalyst. (a) Polarization and power density curves of H_2/O_2 HEMFC with Pt/TRNO (0.4 $mg_{Pt}·cm^{-2}$) in cathode and Pt/C (0.4 $mg_{Pt}·cm^{-2}$) in anode. The cell, cathode, and anode humidifier temperatures were 80, 78, and 79 °C, respectively. The anode and cathode were flowed with 1.0 $L·min^{-1}$ of H_2 and 1.0 $L·min^{-1}$ of O_2, respectively. The backpressures were 200 kPa (gauge) for both sides. (b) Cell voltage during the long-term durability test at a constant current density of 500 $mA·cm^{-2}$. The MEA and test conditions were identical to that in all, except for the flow rate of anode and cathode were both 0.4 $L·min^{-1}$ and the backpressures were 150 kPa (gauge) for both sides.

always exhibits unsatisfied performances, due to the lower conductivity and worse dispersion of the oxide supports. Here, we modified the TiO_2 supports with Nb-doped RuO_2 to elevate its conductivity and also optimized the MEA structures to achieve high-performance HEMFCs, and the obtained Pt/TRNO HEMFC displayed the performance surpassed the other reported HEMFC using non-carbon support materials working under similar operating environments.

More importantly, the HEMFC stability was significantly improved when using Pt/TRNO catalyst. The HEMFC stability was evaluated by discharging at a constant current density of 500 $mA·cm^{-2}$ under H_2/O_2 condition. After a 170-h stability test (Fig. 5(b)), the Pt/TRNO HEMFC maintained its voltage with the voltage loss of only 13 mV (about 2.2%). The cell voltage decay rate is 76 $\mu V·h^{-1}$, which is only 2.1% compared with that for Pt/C HEMFC (3600 $\mu V·h^{-1}$). The high frequency resistance (HFR) only increased around 7 mΩ after the 170-h test (Fig. S12 in the ESM). In contrast, the commercial Pt/C HEMFC rapidly degraded after 50 h of test at the same condition (Fig. 2(c)). At a higher current density of 1000 $mA·cm^{-2}$, the Pt/TRNO HEMFC is also stable indicating by the negligible voltage loss after 30 h of test (Fig. S13 in the ESM). The high stability of the Pt/TRNO HEMFC is attributed to depressed H_2O_2 generation rate by supporting Pt on TRNO, which decreases the chemical degradation of HEM.

4 Conclusion

In summary, we confirmed that the *in-situ* generated H_2O_2 significantly induced the degradation of the HEMFCs. To improve the stability of the HEMFCs, an oxide (TRNO) supported Pt catalyst was synthesized and demonstrated low H_2O_2 yield when catalyzing ORR. A practical HEMFC device was assembled with Pt/TRNO as cathode catalyst, which exhibited outstanding durability. When discharging at a constant current density of 500 $mA·cm^{-2}$, this Pt/TRNO HEMFC only showed 2.2% voltage decay after 170 h of continuous work. This work suggests that the H_2O_2 is one of the key factors determining the HEMFC stability, and the H_2O_2 can be depressed by using oxides as supports, leading to significantly improved HEMFC stability.

Electronic Supplementary Material: Supplementary material (TEM, EDS mapping, BET, XPS, HEMFC performance, etc.) is available in the online version of this article at https://doi.org/10.26599/NR.2025.94907340.

Data availability

All data needed to support the conclusions in the paper are presented in the manuscript and the Electronic Supplementary Material. Additional data related to this paper may be requested from the corresponding author upon request.

Acknowledgements

The authors acknowledge the financial support by the National Key Research and Development Program of China (No. 2019YFA0210300), the National Natural Science Foundation of China (Nos. 22101016 and 22279004), and China National Petroleum Corporation Basic Forward-looking Science and Technology Project (No. 2023ZZ1202).

Declaration of competing interest

All the contributing authors report no conflict of interests in this work.

Author contribution statement

S. X. Z.: Data curation, validation, writing manuscript, experimental design. Y. J. S.: Data curation, Data curation. J. J. F.: Validation, experimental design, funding acquisition. W. Z.: Project administration, validation, writing manuscript, experimental design, funding acquisition. Z. B. Z.: Project administration, validation, writing manuscript, experimental design, funding acquisition. All the authors have approved the final manuscript.

Use of AI statement

None.

References

[1] Gasteiger, H. A.; Marković, N. M. Just a dream-or future reality. *Science* **2009**, *324*, 48–49.

[2] Seh, Z. W.; Kibsgaard, J.; Dickens, C. F.; Chorkendorff, I.; Nørskov, J. K.; Jaramillo, T. F. Combining theory and experiment in electrocatalysis: Insights into materials design. *Science* **2017**, *355*, eaad4998.

[3] Zhu, P.; Xiong, X.; Wang, D. S. Regulations of active moiety in single atom catalysts for electrochemical hydrogen evolution reaction. *Nano Res.* **2022**, *15*, 5792–5815.

[4] Li, W. H.; Yang, J. R.; Wang, D. S. Long-range interactions in diatomic catalysts boosting electrocatalysis. *Angew. Chem., Int. Ed.* **2022**, *61*, e202213318.

[5] Yang, Y. X.; Li, P.; Zheng, X. B.; Sun, W. P.; Dou, S. X.; Ma, T. Y.; Pan, H. G. Anion-exchange membrane water electrolyzers and fuel cells. *Chem. Soc. Rev.* **2022**, *51*, 9620–9693.

[6] Kempler, P. A.; Slack, J. J.; Baker, A. M. Research priorities for seasonal energy storage using electrolyzers and fuel cells. *Joule* **2022**, *6*, 280–285.

[7] Kang, Y. Q.; Wang, J. Q.; Wei, Y. P.; Wu, Y. L.; Xia, D. S.; Gan, L. Engineering nanoporous and solid core–shell architectures of low-platinum alloy catalysts for high power density PEM fuel cells. *Nano Res.* **2022**, *15*, 6148–6155.

[8] Wang, Y.; Ma, F. Y.; Zhang, G. Q.; Zhang, J. W.; Zhao, H.; Dong, Y. M.; Wang, D. S. Precise synthesis of dual atom sites for electrocatalysis. *Nano Res.* **2024**, *17*, 9397–9427.

[9] Zhang, Y. F.; Liu, L. S.; Li, Y. X.; Mu, X. Q.; Mu, S. C.; Liu, S. L.; Dai, Z. H. Strong synergy between physical and chemical properties: Insight into optimization of atomically dispersed oxygen reduction catalysts. *J. Energy Chem.* **2024**, *91*, 36–49.

[10] Chen, F. J.; Mu, X. Q.; Zhou, J. L.; Wang, S. C.; Liu, Z. Y.; Zhou, D. Y.; Liu, S. L.; Wang, D. S.; Dai, Z. H. Engineering the active sites of MOF-derived catalysts: From oxygen activation to activate metal-air batteries. *Chin. J. Chem.* **2024**, *42*, 2520–2535.

[11] Wang, S. C.; Zhang, M. Y.; Mu, X. Q.; Liu, S. L.; Wang, D. S.; Dai, Z. H. Atomically dispersed multi-site catalysts: Bifunctional oxygen electrocatalysts boost flexible zinc-air battery performance. *Energy Environ. Sci.* **2024**, *17*, 4847–4870.

[12] Setzler, B. P.; Zhuang, Z. B.; Wittkopf, J. A.; Yan, Y. S. Activity targets for nanostructured platinum-group-metal-free catalysts in hydroxide exchange membrane fuel cells. *Nat. Nanotechnol.* **2016**, *11*, 1020–1025.

[13] Dekel, D. R. Review of cell performance in anion exchange membrane fuel cells. *J. Power Sources* **2018**, *375*, 158–169.

[14] Xin, D. Y.; Liu, X. R.; Chen, B. W.; Jin, X. X.; Hao, J. Y.; Wang, Y. X.; Hu, R. B.; Fu, J. C.; Wang, S. Z.; Zhu, W. et al. *In situ*-grown ultrathin catalyst layers for improving both proton exchange membrane fuel cell and anion exchange membrane fuel cell performances. *ACS Appl. Mater. Interfaces.* **2024**, *16*, 42363–42371.

[15] Yang, C. M.; Zhang, L.; Lu, Y. X.; Zou, Y. Q.; Wang, S. Y. Designing efficient catalysts for electrocatalytic organic synthesis: From electronic structure to adsorption behavior. *Matter* **2024**, *7*, 456–474.

[16] Liu, X. R.; Wang, X. D.; Zhang, C. Y.; Cai, Y.; Chen, B. W.; Xin, D. Y.; Jin, X. X.; Zhu, W.; Wippermann, K.; Li, H. et al. The difference of the ionomer-catalyst interfaces for poly(aryl piperidinium) hydroxide exchange membrane fuel cells and proton exchange membrane fuel cells. *Nano Res.* **2024**, *17*, 6102–6110.

[17] Mustain, W. E.; Chatenet, M.; Page, M.; Kim, Y. S. Durability challenges of anion exchange membrane fuel cells. *Energy Environ. Sci.* **2020**, *13*, 2805–2838.

[18] Ul Hassan, N.; Mandal, M.; Huang, G.; Firouzjaie, H. A.; Kohl, P. A.; Mustain, W. E. Achieving high‐performance and 2000 h stability in anion exchange membrane fuel cells by manipulating ionomer properties and electrode optimization. *Adv. Energy Mater.* **2020**, *10*, 2001986.

[19] Ul Hassan, N.; Zachman, M. J.; Mandal, M.; Adabi Firouzjaie, H.; Kohl, P. A.; Cullen, D. A.; Mustain, W. E. Understanding recoverable vs unrecoverable voltage losses and long-term degradation mechanisms in anion exchange membrane fuel cells. *ACS Catal.* **2022**, *12*, 8116–8126.

[20] Li, H. Y.; Cheng, X. J.; Yan, X. H.; Shen, S. Y.; Zhang, J. L. A perspective on influences of cathode material degradation on oxygen transport resistance in low Pt PEMFC. *Nano Res.* **2023**, *16*, 377–390.

[21] Li, N. W.; Leng, Y. J.; Hickner, M. A.; Wang, C. Y. Highly stable, anion conductive, comb-shaped copolymers for alkaline fuel cells. *J. Am. Chem. Soc.* **2013**, *135*, 10124–10133.

[22] Lee, W. H.; Kim, Y. S.; Bae, C. Robust hydroxide ion conducting poly(biphenyl alkylene)s for alkaline fuel cell membranes. *ACS Macro Lett.* **2015**, *4*, 814–818.

[23] Kuroki, H.; Miyanishi, S.; Sakakibara, A.; Oshiba, Y.; Yamaguchi, T. Highly stable membrane-electrode assembly using ether-linkage-free spirobifluorene-based aromatic polyelectrolytes for direct formate solid alkaline fuel cells. *J. Power Sources* **2019**, *438*, 226997.

[24] Lim, H. J.; Kim, G.; Yun, G. J. Durability and performance analysis of polymer electrolyte membranes for hydrogen fuel cells by a coupled chemo-mechanical constitutive model and experimental validation. *ACS Appl. Mater. Interfaces* **2023**, *15*, 24257–24270.

[25] Peng, X.; Kulkarni, D.; Huang, Y.; Omasta, T. J.; Ng, B.; Zheng, Y. W.; Wang, L. Q.; LaManna, J. M.; Hussey, D. S.; Varcoe, J. R. et al. Using *operando* techniques to understand and design high performance and stable alkaline membrane fuel cells. *Nat. Commun.* **2020**, *11*, 3561.

[26] Thomas, O. D.; Soo, K. J. W. Y.; Peckham, T. J.; Kulkarni, M. P.; Holdcroft, S. A stable hydroxide-conducting polymer. *J. Am. Chem. Soc.* **2012**, *134*, 10753–10756.

[27] Wright, A. G.; Fan, J. T.; Britton, B.; Weissbach, T.; Lee, H. F.; Kitching, E. A.; Peckham, T. J.; Holdcroft, S. Hexamethyl-p-terphenyl poly(benzimidazolium): A universal hydroxide-conducting polymer for energy conversion devices. *Energy Environ. Sci.* **2016**, *9*, 2130–2142.

[28] Hu, C.; Kang, H. W.; Jung, S. W.; Zhang, X. H.; Lee, Y. J.; Kang, N. Y.; Park, C. H.; Lee, Y. M. Stabilizing the catalyst layer for durable and high performance alkaline membrane fuel cells and water electrolyzers. *ACS Cent. Sci.* **2024**, *10*, 603–614.

[29] Germer, W.; Leppin, J.; Kirchner, C. N.; Henkensmeier, D.; Dyck, A. TGA-GC/MS—An adjuvant tool for analysis of polymer membranes designed for fuel cell use. *Procedia Eng.* **2012**, *44*, 1310–1314.

[30] Su, X. D.; Gao, L.; Hu, L.; Qaisrani, N. A.; Yan, X. M.; Zhang, W. J.; Jiang, X. B.; Ruan, X. H.; He, G. H. Novel piperidinium functionalized anionic membrane for alkaline polymer electrolysis with excellent electrochemical properties. *J. Membr. Sci.* **2019**, *581*, 283–292.

[31] Mohanty, A. D.; Ryu, C. Y.; Kim, Y. S.; Bae, C. Stable elastomeric anion exchange membranes based on quaternary ammonium-tethered polystyrene-b-poly(ethylene-co-butylene)-b-polystyrene triblock copolymers. *Macromolecules* **2015**, *48*, 7085–7095.

[32] Fan, J. T.; Wright, A. G.; Britton, B.; Weissbach, T.; Skalski, T. J. G.; Ward, J.; Peckham, T. J.; Holdcroft, S. Cationic polyelectrolytes, stable in 10 M KOH_{aq} at 100 °C. *ACS Macro Lett.* **2017**, *6*, 1089–1093.

[33] Wang, J. H.; Zhao, Y.; Setzler, B. P.; Rojas-Carbonell, S.; Ben Yehuda, C.; Amel, A.; Page, M.; Wang, L.; Hu, K. D.; Shi, L. et al. Poly(aryl piperidinium) membranes and ionomers for hydroxide exchange membrane fuel cells. *Nat. Energy* **2019**, *4*, 392–398.

[34] Okonkwo, P. C.; Ben Belgacem, I.; Emori, W.; Uzoma, P. C. Nafion degradation mechanisms in proton exchange membrane fuel cell (PEMFC) system: A review. *Int. J. Hydrogen Energy* **2021**, *46*, 27956–27973.

[35] Zhao, D.; Yi, B. L.; Zhang, H. M.; Liu, M. L. The effect of platinum in a Nafion membrane on the durability of the membrane under fuel cell conditions. *J. Power Sources* **2010**, *195*, 4606–4612.

[36] Choi, C. H.; Kwon, H. C.; Yook, S.; Shin, H.; Kim, H.; Choi, M. Hydrogen peroxide synthesis via enhanced two-electron oxygen reduction pathway on carbon-coated Pt surface. *J. Phys. Chem. C* **2014**, *118*, 30063–30070.

[37] Eslamibidgoli, M. J.; Melchy, P. É. A.; Eikerling, M. H. Modeling the local potential at Pt nanoparticles in polymer electrolyte membranes. *Phys. Chem. Chem. Phys.* **2015**, *17*, 9802–9811.

[38] Espiritu, R.; Golding, B. T.; Scott, K.; Mamlouk, M. Degradation of radiation grafted hydroxide anion exchange membrane immersed in neutral pH: Removal of vinylbenzyl trimethylammonium hydroxide due to oxidation. *J. Mater. Chem. A* **2017**, *5*, 1248–1267.

[39] Zhang, Y. Z.; Parrondo, J.; Sankarasubramanian, S.; Ramani, V. Detection of reactive oxygen species in anion exchange membrane fuel cells using *in situ* fluorescence spectroscopy. *ChemSusChem* **2017**, *10*, 3056–3062.

[40] Verdaguer-Casadevall, A.; Deiana, D.; Karamad, M.; Siahrostami, S.; Malacrida, P.; Hansen, T. W.; Rossmeisl, J.; Chorkendorff, I.; Stephens, I. E. L. Trends in the electrochemical synthesis of H_2O_2: Enhancing activity and selectivity by electrocatalytic site engineering. *Nano Lett.* **2014**, *14*, 1603–1608.

[41] Lu, Z. Y.; Chen, G. X.; Siahrostami, S.; Chen, Z. H.; Liu, K.; Xie, J.; Liao, L.; Wu, T.; Lin, D. C.; Liu, Y. Y. et al. High-efficiency oxygen reduction to hydrogen peroxide catalysed by oxidized carbon materials. *Nat Catal.* **2018**, *1*, 156–162.

[42] Sun, S. H.; Yang, D. Q.; Villers, D.; Zhang, G. X.; Sacher, E.; Dodelet, J. P. Template- and surfactant-free room temperature synthesis of self-assembled 3D Pt nanoflowers from single-crystal nanowires. *Adv. Mater.* **2008**, *20*, 571–574.

[43] Xiao, F.; Wang, Y. C.; Wu, Z. P.; Chen, G. Y.; Yang, F.; Zhu, S. Q.; Siddharth, K.; Kong, Z. J.; Lu, A. L.; Li, J. C. et al. Recent advances in electrocatalysts for proton exchange membrane fuel cells and alkaline membrane fuel cells. *Adv. Mater.* **2021**, *33*, 2006292.

[44] Yang, Y.; Peltier, C. R.; Zeng, R.; Schimmenti, R.; Li, Q. H.; Huang, X.; Yan, Z. F.; Potsi, G.; Selhorst, R.; Lu, X. Y. et al. Electrocatalysis in alkaline media and alkaline membrane-based energy technologies. *Chem. Rev.* **2022**, *122*, 6117–6321.